

See discussions, stats, and author profiles for this publication at: <https://www.researchgate.net/publication/263013163>

Study on Mn-induced Jahn–Teller distortion in BiFeO₃ thin films

ARTICLE *in* JOURNAL OF MATERIALS SCIENCE · SEPTEMBER 2014

Impact Factor: 2.37 · DOI: 10.1007/s10853-014-8318-9

CITATIONS

2

READS

27

3 AUTHORS:



Surbhi Gupta

Kyushu Institute of Technology, Frontier R ...

10 PUBLICATIONS 22 CITATIONS

SEE PROFILE



Monika Tomar

University of Delhi

136 PUBLICATIONS 667 CITATIONS

SEE PROFILE



Vinay Gupta

University of Delhi

263 PUBLICATIONS 3,672 CITATIONS

SEE PROFILE

Study on Mn-induced Jahn–Teller distortion in BiFeO₃ thin films

Surbhi Gupta · Monika Tomar · Vinay Gupta

Received: 18 March 2014 / Accepted: 9 May 2014 / Published online: 28 May 2014
© Springer Science+Business Media New York 2014

Abstract Present work reports Raman spectroscopy study of single-phase Mn-doped BiFeO₃ [BiFe_{1-x}Mn_xO₃ ($0 \leq x \leq 0.20$)] polycrystalline thin films carried out in backscattering geometry. De-convolution of Raman spectra showed a gradual transition in the crystal symmetry from rhombohedral (–R) to multiphase [rhombohedral (–R) + tetragonal (–T)] structure with increasing Mn doping concentration in BiFe_{1-x}Mn_xO₃ (BFMO) thin films. X-ray diffraction (XRD) along with Le-Bail extraction refinement confirms that the structural symmetry lowering in BFMO thin films occurs at about 10 % Mn doping concentration. A blue shift is observed in the direct energy band gap of BFMO thin films from 2.53 to 2.87 eV (at $T = 295$ K) and is attributed to the local symmetry lowering and local induced strain in Fe³⁺ environment resulted from Jahn–Teller distortion in (MnFe)³⁺O₆ octahedral unit. Second-derivative analysis of FTIR spectra in the spectral regions (420–470) cm^{–1} and (480–680) cm^{–1} further indicates the favourable structure distortion leading to the simultaneous exhibition of enhanced ferromagnetic and ferroelectric properties owing to Mn substitution in host BiFeO₃ lattice.

Introduction

Multiferroic thin films are providing a new dimension to industrial applications such as magnetic sensors, quantum

electro-magnets, tunnel magneto-resistance (TMR) sensors and spin valves with electric field tunable functions and high density magnetically read electrically written non-destructive low-power storage devices with multiple state memory (MERAMs) [1–3]. Photovoltaic properties of multiferroic oxides thin films are of great importance in search of appropriate materials towards renewable energy harvesting [4]. Among various multiferroic compounds, BiFeO₃ (BFO) is a promising perovskite (ABO₃) material which combines both ferromagnetic order (weak/Anti-ferromagnetism) and ferroelectric order parameters at room temperature in the same phase [3]. BFO also exhibits other exotic properties including small and direct energy band gap and strong absorption coefficient in visible range and anomalous photovoltaic effect besides magneto-electric (ME) coupling making it an apparent choice for ultrafast optoelectronic devices, ferroelectric photovoltaic solar cell, photo-catalytic material actuators, etc. [4–6].

However, utilization of BFO thin films for functional devices is still challenging owing to the presence of defects and non-stoichiometry, due to Bi volatility and relative valance fluctuation of Fe ions causing high leakage current density and poor polarization [3]. Physical properties are sensitive to the changes in crystallographic structure, and thus efforts are continuing towards improving the ferroelectric as well as magnetic properties of BFO thin films by material engineering through A (Bi–) or B (Fe–) site substitutions which leads to favourable structure distortion [7–10]. Raman spectroscopy is known to be a sensitive technique to study the structural distortion and defects in thin films [7, 10]. Size, temperature and field dependent variations in vibrational phonon modes of BiFeO₃ nanoparticles and single crystal have been studied [11–13]. Lattice dynamic properties using first-principle calculations of rhombohedral phase and tetragonal phase of BiFeO₃ have

S. Gupta · V. Gupta (✉)
Department of Physics and Astrophysics, University of Delhi,
Delhi, India
e-mail: drguptavinay@gmail.com

M. Tomar
Physics Department, Miranda House, University of Delhi, Delhi,
India

also been reported [14, 15]. However, limited reports are available which have studied changes in lattice dynamic properties of doped BFO thin films with increasing dopant concentration [16–18]. Lack of correlation among the Raman and FTIR spectroscopy study and distortion in the crystallographic structure and correspondingly induced ferroelectric behaviour of doped BFO thin films is the motivating factor for this detailed report. Allibe et al. [4] and Chen et al. [5] have studied optical properties of BFO thin film deposited on various epitaxially matched substrates including (001) MgO, (001)/(111) SrTiO₃ and (110) YAlO₃ using pulsed laser deposition and laser molecular-beam epitaxy technique, respectively. Also, rare earth (Nd, Ce) substitution in BFO thin films has resulted in an increase in optical energy band gap [6, 19]. Although Mishra et al. [20] have studied influence of transition metal (Ni) doping on photoluminescence and transmittance of sol-gel-derived BFO thin films, detailed discussion of origin of variation in optical behaviour is yet to be carried out. In the present study, BiFe_{1-x}Mn_xO₃ (x varying from 0 to 0.20) thin films have been deposited on cost-effective corning glass and indium tin oxide (ITO)-coated glass substrates using a simple chemical solution deposition (CSD) technique and the influence of varying Mn doping concentration on the structural distortion, vibrational phonon modes and optical properties of BFO thin films has been investigated systematically.

Experimental

BFMO thin films of thickness 350 nm were grown by CSD technique on corning glass (7059) and ITO-coated corning glass substrates by CSD technique. 0.2 M stock precursor solutions having different compositions of BiFe_{1-x}Mn_xO₃ with varying ($x = 0, 0.05, 0.1, 0.15$ and 0.20) were prepared by dissolving high purity (>99 %) source material including bismuth(III) nitrate pentahydrate {Bi(NO₃)₃·5H₂O}, iron(III) nitrate nanohydrate {Fe(NO₃)₃·9H₂O} and manganese(II) acetate tetrahydrate {C₄H₆MnO₄·4H₂O} in 2-methoxy ethanol {CH₃OCH₂CH₂OH} and glacial acetic acid {CH₃COOH}. It has been observed that the ferroic properties of BFO thin films are very sensitive to the excess bismuth content. 5 mol% excess Bi content is also incorporated in all stock solutions to maintain the stoichiometry and compensate the Bi loss during annealing process at high temperature owing to high Bi volatility. Precursor solution preparation details and thin film deposition parameters have been reported in our earlier communication [21]. All deposited BFMO thin films are annealed in inert N₂ gas atmosphere for 45 min at 550 °C to enhance the crystallinity and subdue the oxygen vacancy defects.

Thickness of deposited thin films was measured using a surface profiler (Veeco, Dektak 150). Crystallographic structure and phase transition of BFMO thin films were studied using X-ray diffractometer (Bruker, D8 Discover). XRD patterns of the prepared thin film samples were obtained in 2θ range from 20° to 70° using Cu K α radiation source. Raman spectroscopy measurements were performed in the backscattering geometry using a Renishaw InVia Reflex Micro Raman spectrophotometer. Radiation at 514 nm from air cooled Ar⁺ ion laser was incident on the surface of thin film samples along the normal. Accumulation time of the spectrum, slit width (2,400 grooves/mm grating) and laser beam power were adjusted to have high signal-to-noise ratio. Optical transmission spectra of all BFMO thin films deposited onto corning glass substrates were recorded using UV–visible spectrophotometer (Perkin-Elmer, Lambda 35) in the wavelength region 190–1100 nm. Fourier transform infrared (FTIR) spectra were obtained using (Perkin-Elmer, Frontier) spectrophotometer at resolution of 4 cm⁻¹ in the mid-IR spectral range (400–1000 cm⁻¹) using HgCdTe detector.

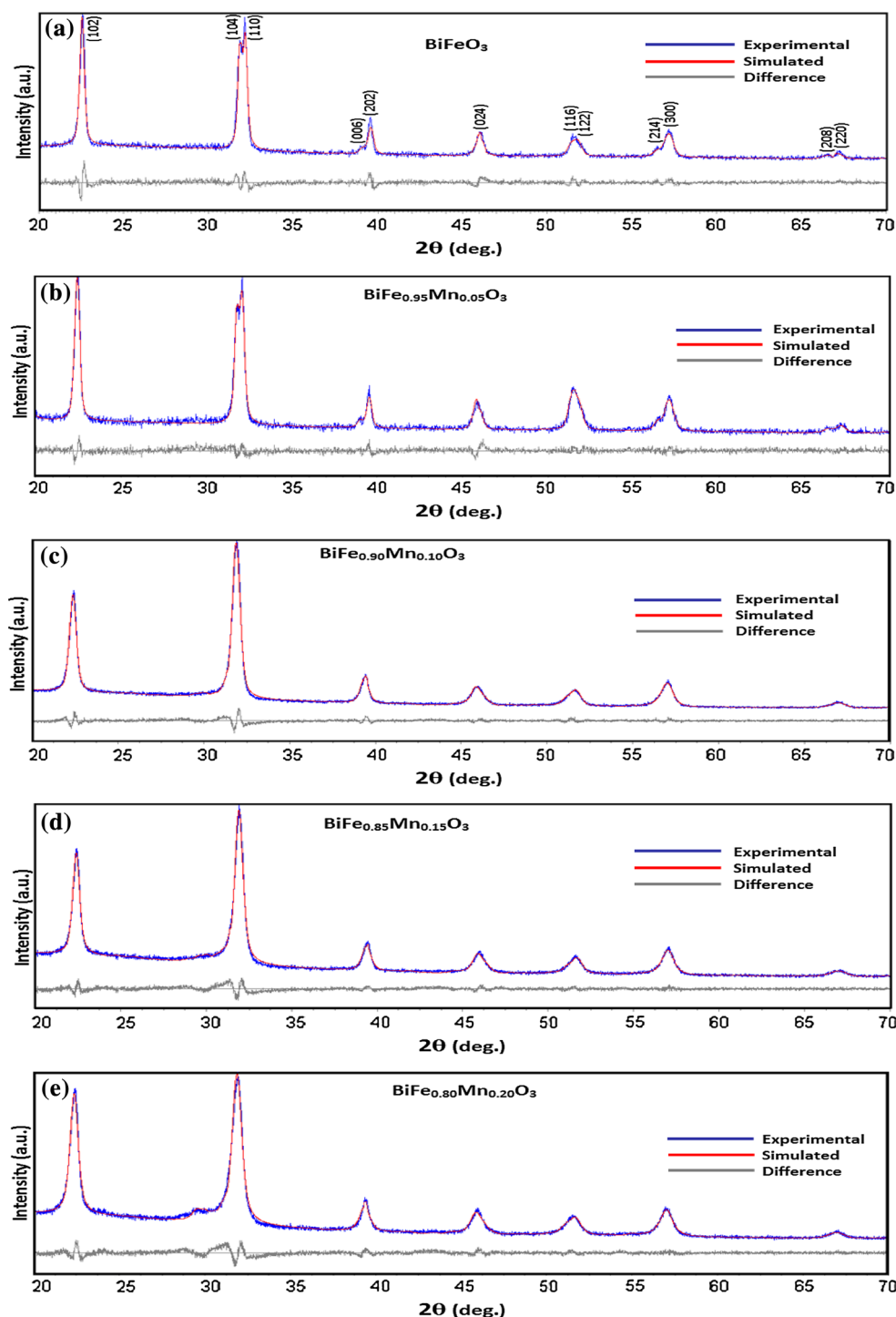
Results and discussion

Structural Analysis

XRD patterns of BiFe_{1-x}Mn_xO₃ (BFMO) thin films with $x = 0, 0.05, 0.10, 0.15$ and 0.20 recorded in Bragg–Brentano $\theta/2\theta$ configuration are shown in Fig. 1a–e, respectively. XRD patterns obtained for each BFMO thin film were also simulated using LeBail intensity extraction method with the help of Bruker TOPAS 3 software, and various structural parameters have been determined. The best fitted theoretical XRD curve and the difference curve indicating error between the experimental and simulated XRD pattern are also shown in respective Fig. 1a–e for all prepared BFMO samples. All reflections are indexed in the XRD pattern of BFO thin film (Fig. 1a) based on the perovskite-type structure which is in good agreement with International Centre of Diffraction Data (ICDD card no. 00-020-0169) and shows the formation of rhombohedral distorted structure (space group R3c) with no trace of impurity phases such as Bi₂O₃ and Fe₂O₃ within the limitation of XRD [20, 21]. The XRD data also confirm that polycrystalline BiFe_{1-x}Mn_xO₃ thin films synthesized without any secondary phase till $x = 0.10$ beyond which diffraction peak of secondary phase start appearing at around $2\theta = 30^\circ$ due to excess Mn doping (Fig. 1d–e).

It may be observed from Fig. 1 that the intensity of (110/104) diffraction peak is increased for BFMO thin films in comparison to BFO thin film. Intensity of the (110/104) diffraction peak is found to be stronger than that of the

Fig. 1 XRD pattern of $\text{BiFe}_{1-x}\text{Mn}_x\text{O}_3$ thin films with $x = \mathbf{a}$ 0, **b** 0.05, **c** 0.1, **d** 0.15 and **e** 0.20. The Le-Bail Refinement along with difference curves between experimental data and best fitting are also shown



(012) diffraction peak in BFO thin film sample with $x = 0.10$, suggested a preferred crystallite orientation along the (110) direction while such texture orientation seems to be weakened in 15 and 20 % Mn-doped BFO thin film samples (Fig. 1c–e). Increasing Mn substitution in host BFO lattice is found to break symmetry from rhombohedral ($R3c$) to lower symmetry, as lattice distortion is clearly observed by overlapping of the characteristic

splitting of (104), (006), (214), and (208) diffraction peaks (visible for BFO thin film) at $2\theta = 32^\circ$, 40° , 56.8° and 66° respectively in Fig. 1b–e [22]. Increasing substitution of Mn at Fe sites in BFO host lattice also resulted in the continuous shifting of (104), (024) and (116) XRD peaks towards higher angle (explicitly shown elsewhere) [21] and further indicates gradual phase transition to lower symmetry which is beneficial for improving the ferroelectric as

Table 1 Various structural parameters including (“a” and “c”), cell volume, crystallite size and lattice distortion (c/a) for the BFMO thin films with varying Mn doping concentration

Sample name	$a = b$ (Å)	c (Å)	Crystallite size (Å)	c/a distortion value	$V(\text{Å}^3)$	R values			$S = R_{\text{WP}}/R_{\text{EXP}}$
						R_{P} (%)	R_{WP} (%)	R_{EXP} (%)	
BiFeO ₃	5.618	6.940	220	1.2353	187.744	5.47	5.67	4.81	1.18
BiFe _{0.95} Mn _{0.05} O ₃	5.567	6.899	174	1.2393	185.720	10.26	13.08	11.14	1.17
BiFe _{0.9} Mn _{0.1} O ₃	5.549	6.889	167	1.2415	184.471	7.22	8.81	7.53	1.18
BiFe _{0.85} Mn _{0.15} O ₃	5.547	6.883	162	1.2408	183.730	5.22	6.58	5.48	1.2
BiFe _{0.80} Mn _{0.20} O ₃	5.546	6.881	161	1.2407	183.462	5.23	6.52	5.44	1.2

Corresponding R -factors and goodness of fitting factor “s” is also included

well as magnetic properties [7, 10, 21]. It is important to point out that for BFMO thin films having higher Mn doping concentration ($\geq 10\%$), the best fit of XRD data using Le-Bail fitting is obtained only for tetragonal structure with P4 mm space group shown in Fig. 1c–e indicating a partial phase transformation from rhombohedral to tetragonal structure. The difference curves shown in Fig. 1a–e suggest that theoretically simulated XRD patterns match well with the experimentally obtained XRD patterns for all prepared samples. The values of lattice parameters (“a” and “c”), cell volume (V) and “c/a” distortion factor extracted from the simulation of XRD data and corresponding R -factors are tabulated in Table 1. The fitting parameters are chosen such that R -factors are small, and the goodness of fitting value “s” is less than 1.2 as shown in Table 1. Significant decrease in lattice constants (“a” and “c”) and, hence, the contraction in unit cell is observed with increasing Mn doping concentration (Table 1) which is attributed to the substitution of Mn^{3+} ion of smaller ionic radii (0.645 Å) at the Fe^{3+} ions sites with larger ionic radius (0.782 Å) in BFO host lattice [21].

However, “c/a” distortion ratio increases significantly from 1.235 to 1.242 with increase in Mn dopant concentration from 0 to 10 % in BFMO thin films and reduces thereafter at higher Mn doping percentage ($>10\%$) similar to that observed for unit cell volume (Table 1). The observed partial structural transformation from rhombohedral to tetragonal phase with high distortion ratio (1.242) for $\text{BiFe}_{0.9}\text{Mn}_{0.1}\text{O}_3$ thin film is related to the size effect also known as tolerance factor which arise due to larger ionic radius mismatch between r_A and r_B upon doping of Mn ion in BFO (ABO_3) perovskite host lattice, favourable for exhibiting improved ferroelectric behaviour. It may also be seen from Fig. 1a–e that both the intense (102) and (110) diffraction peaks are substantially broadened with increasing Mn content till ($x = 0.10$), and thereafter not much increase in FWHM is observed for higher Mn doping content ($\geq 15\%$). Average crystallite size of BFMO thin films calculated from Debye–Scherrer’s formula is found to be decreasing from 22 to 16 nm with increase in Mn

doping concentration from 0 to 20 % (Table 1). The observed tendency is may be due to the incorporation of Mn rather at the interstitial sites in BFO lattice for higher Mn doping ($\geq 15\%$) concentration as evidenced by the occurrence of secondary phases (Fig. 1c–e) which lead to the degradation of ferroelectric properties. It may infer that 10 % Mn substitution in host BFO lattice near the phase boundary composition led to favourable lattice distortion from rhombohedral to multiphase [rhombohedral (R) + tetragonal (T)] structure with the largest tetragonal distortion ratio (1.241) and different (110) preferred orientations. Crystallites oriented along (111) direction exhibit enhanced ferroelectric properties, while oriented along (110) direction possess maximum projection along the (111) direction compared to the other orientations and hence contribute maximum to spontaneous polarization [22] which resulted into enhanced ferroelectric properties and magnetic properties at room temperature shown in previous work due to increased canting of magnetic spin moments due to coupling with enhanced polarization and the destruction of the spin cycloid structure in BFO thin film [21].

Raman Spectra Analysis

Raman scattering spectra are sensitive to atomic displacements and the evolvment of vibrational phonon modes with increasing Mn dopant concentration in BFO thin film can provide valuable information about lattice distortion. All Raman active transverse (TO) and longitudinal (LO) vibrational lattice modes in BFMO thin film samples are identified by de-convoluting the experimentally obtained Raman spectra into the Gaussian components and are shown in Fig. 2a–e for varying doping concentration of Mn from 0 to 20 % respectively. Group theory predicts 18 optical phonon modes ($\Gamma = 4A_1 + 5A_2 + 9E$) for rhombohedral ($-R$) phase of BFO, out of which only 13 modes ($4A_1 + 9E$) are both Raman active and IR active while four A_2 modes are silent [13–15, 23]. All 13 active modes observed in the Raman spectra of BFO thin film ($-R$)

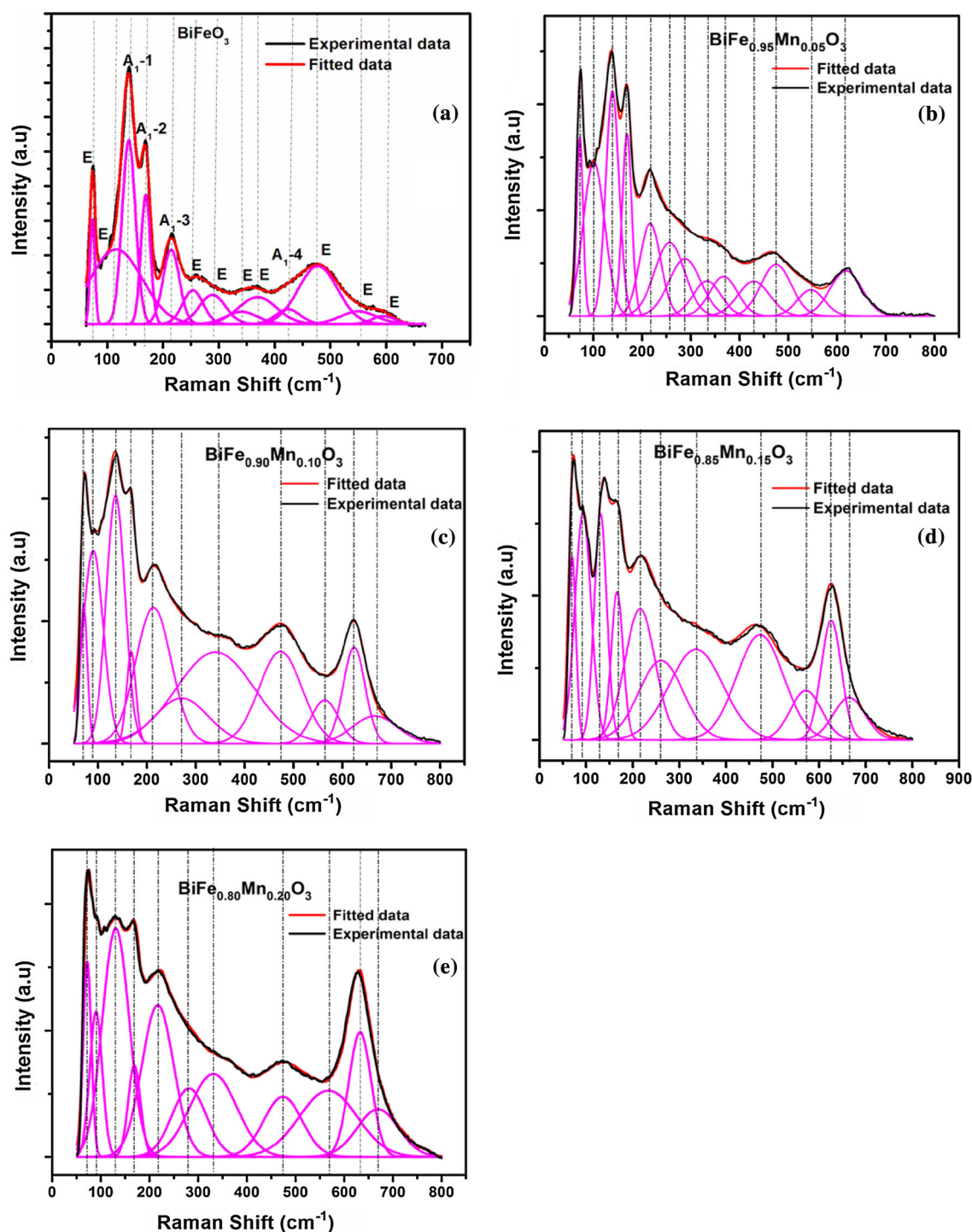


Fig. 2 Raman spectra along with de-convoluted Raman active modes for $\text{BiFe}_{1-x}\text{Mn}_x\text{O}_3$ thin film samples with **a** $x = 0.0$, **b** $x = 0.05$, **c** $x = 0.1$, **d** $x = 0.15$, **e** $x = 0.20$. Broken standing lines represent the position of different Raman modes of BFMO thin film samples

phase listed in Table 2 are found to match well with the earlier reported results [15, 23]. The obtained phonon modes after deconvoluting the Raman spectra of all BFMO thin films with ($x = 0.05$ to 0.2) are also summarized in Table 2.

It may be seen from Fig. 2a–c and Table 2 that low-frequency Raman modes observed at 71 cm^{-1} ($E - 1$), 136 cm^{-1} ($A_1 - 1$) and 167 cm^{-1} ($A_1 - 2$) are well defined and intense for BFMO samples till low Mn doping concentration ($\leq 10\%$). However, all these modes become

Table 2 Comparison of identified Raman modes (cm^{-1}) from the present work and literature

	Raman modes (R phase)	Kothari et al. [23]	$X = 0$	$X = 0.05$	$X = 0.10$	$X = 0.15$	$X = 0.2$	Tütüncü et al. [15]	Singh et al. [24]	Raman modes (T phase)
Low-frequency modes	E	71	71	71	70	70	70			
	E	98	107	101	97	94	91	96	125	E
	A_1	135	136	133	129	126	124	237	129	A_1
	A_1	167	167	167	167	167	167	427	155	A_1
Mid-frequency modes	A_1	218	215	215	216	216	216		206	A_1
	E	255	253	258	264	270	277	207	245	E
	E	283	288	286	–	–	–			
	E	321	341	336	333	330	328	332	332	B_1
	E	351	366	366	–	–	–			
High-frequency modes	A_1	430	433	434	661	663	665	662		A_1
	E	467	478	476	475	475	476	357	453	E
	E	526	546	555	560	566	571			
	E	598	601	617	621	625	628	612	530	E

broad and their intensity was found to decrease greatly (Fig. 2d–e) with higher Mn doping concentration ($>10\%$), which indicates reduced ferroelectric (FE) behaviour in 15 and 20 % Mn-doped BFO thin films, as also reported in earlier communication [21]. It is the well-known fact verified experimentally and theoretically as well that FE order of BFO is largely governed by Bi–O bond vibration and stereochemically active $6s^2$ lone pair of Bi^{3+} , which participate only in low wavenumber phonon modes ($<167\text{ cm}^{-1}$) as they form rigid perovskite layer of heavier atoms [12]. Moreover, continuous shift towards lower wavenumber is also observed in the Raman modes E-2 (107 cm^{-1} to 91 cm^{-1}) and $A_1 - 1$ (136 to 124 cm^{-1}) with increase in Mn doping concentration from 0 to 20 % (Table 2). Such shift is attributed to continuous deformation of the chemical bonds and symmetry of the BFO lattice with Mn incorporation to the tetragonal phase. In support, 8 Raman active modes reported for tetragonal P4mm phase of BFO summarized as ($\Gamma = 3A_1 + B_1 + 4E$) are also listed in Table 2 for comparative study [15, 24]. Tütüncü et al. [15] and Singh et al. [24] have reported E mode at 96 cm^{-1} and A_1 mode at 129 cm^{-1} for tetragonal structure of BFO thin films and are found to be in agreement with the observed shift in E-2 and $A_1 - 1$ modes in the present case for BFMO thin films having 10 % Mn dopant (Table 2), which confirms the partial phase transition from rhombohedral to tetragonal structure.

With increasing Mn doping substitution, a continuous shift in the mid-frequency phonon mode E-3 towards higher wavenumber (253 cm^{-1} to 277 cm^{-1}) is also observed, while Raman mode E-5 shows a shift towards lower wavenumber from 341 cm^{-1} to 328 cm^{-1} (Table 2). Peak position of E-5 mode in Raman spectra of BFMO thin film samples with ($x \leq 0.05$) is in good agreement with the

corresponding reports on rhombohedral phase of BFO [23], while at higher Mn concentration ($\geq 10\%$), peak position of E-5 mode becomes close to reported peak position of Raman mode B_1 for tetragonal structure of BFO [15]. E-4 and E-6 Raman modes observed at 288 cm^{-1} and 366 cm^{-1} and governed by atomic vibration in oxygen plane [25] are found to be broadened till 5 % Mn doping in BFO thin films (Table 2). The obtained results indicate shorter phonon lifetime because of the smaller crystallite sizes (Table 1) and decrease in defects such as oxygen vacancies [26]. However, E-4 and E-6 Raman active modes disappear for the BFMO thin films having higher Mn ($\geq 10\%$) concentration.

High-frequency Raman phonon modes are strongly dominated by vibrational and rotational motion of FeO_6 octahedra [27]. The occurrence of multiphase [rhombohedral ($-R$) + tetragonal ($-T$)] structure in tetragonal structure of BFMO film at higher Mn doping concentration ($\geq 10\%$) is clearly evidenced by an abrupt disappearance of A_1 -4 mode signifying rhombohedral structure centred at 433 cm^{-1} followed by emergence of a weak band at 661 cm^{-1} assigned as A_1 mode of tetragonal structure (Table 2) and is consistent with other reports [15]. However, E-7 mode centred at 478 cm^{-1} does not show any significant shift with change in Mn doping concentration. The relative intensity of E-7 mode is found to be increasing for BFMO thin film samples in comparison to other lower frequency E phonon modes till 10 % Mn doping concentration and thereafter starts decreasing (till 20 % Mn doping). A continuous shift towards higher wavenumber is observed in both Raman modes E-8 and E-9 from 546 cm^{-1} to 571 cm^{-1} and 601 cm^{-1} to 628 cm^{-1} , respectively (Fig. 2b–e). Increase in intensity of E-7 and E-9 modes is attributed to the enhancement in Jahn–Teller

distortion of $(\text{Mn,Fe})^{3+}\text{O}_6$ octahedra originated from symmetric and anti-symmetric stretching and bending of Mn^{3+}O_6 octahedra [28]. Moreover, the observed shift in E-9 mode is attributed to various local factors, such as the force constant and ionic mass of the substitutive elements. The frequency of phonon mode is proportional to $(k/M)^{1/2}$, where k is the force constant related to bond strength and ionic radii of the constituent ion and M is the reduced mass of the mode [5]. Since the ionic radius of Mn^{3+} ion (0.645 Å) substituting Fe^{3+} ions (0.782 Å) is relatively much smaller, force constant is expected to increase after Mn substitution in BFO lattice. Moreover, the effective mass of Mn^{3+} ion is also small in compare to Fe^{3+} ion, thus doping of relatively lighter Mn^{3+} ion may further caused the shift in E-9 phonon mode towards higher frequency. These observations indicate that more than 10 % Mn doping in BFMO thin films degrades the ferroelectric behaviour.

UV–visible transmission study

Optical transmission spectra of $\text{BiFe}_{1-x}\text{Mn}_x\text{O}_3$ ($x = 0.00, 0.05, 0.10, 0.15$ and 0.20) thin films acquired in wavelength range 190 to 1100 nm are shown in Fig. 3. It may be seen from Fig. 3 that the BFO thin film sample is highly transparent ($>75\%$) in the visible region having a well-defined fundamental absorption edge at around $\lambda = 430$ nm which is in good agreement to the typical UV–vis transmittance spectra obtained for BFO reported elsewhere [6, 15]. However, with increasing incorporation of Mn dopant, the optical transmittance of BFMO thin

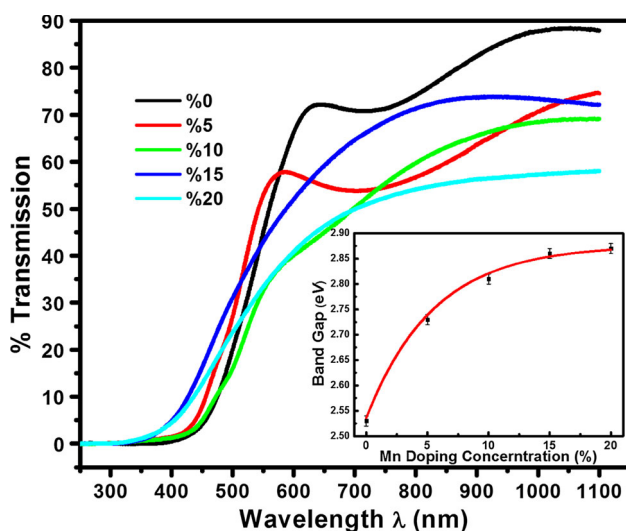


Fig. 3 UV–visible transmission spectra obtained for $\text{BiFe}_{1-x}\text{Mn}_x\text{O}_3$ thin films with varying concentration of Mn dopant from 0 to 0.20. Inset shows the variation in band gap of BFMO thin films as a function of Mn doping concentration

films decreases and a gradual absorption edge shifts towards lower wavelength is observed. The value of energy band gap for different BFMO thin film samples were calculated using the Tauc plot of $(\alpha h\nu)^2$ versus $h\nu$, where α is the absorption coefficient and $h\nu$ is the incident photon energy [6]. Thus, obtained optical energy band gap of BFMO thin films with varying Mn concentration is plotted in the inset of Fig. 3. It may be seen that the value of energy band gap is blue shifted from 2.53 ± 0.01 eV to 2.87 ± 0.01 eV with increase in Mn doping concentration from 0 to 20 %. Energy band gap values estimated in the present work are found to be relatively higher as compared to the corresponding values reported for bulk (1.8–2.3 eV) which is attributed to the small grain size of the deposited BFMO thin films [5].

The observed continuous increase in the band gap of BFMO thin films with increasing Mn doping concentration is attributed to the local structure symmetry lowering as verified by crystal field theory (CFT) [15]. Considering the FeO_6 structure which is ideally an octahedron in rhombohedral BiFeO_3 lattice and each Fe^{3+} centre is coordinated by six O^{2-} ions in R3c space group with distortion along [111] plane [15], and incorporation of Mn at Fe site introduce slight tetragonal distortion. According to CFT, 3d orbitals of Fe ion in FeO_6 octahedron split into t_{2g} and e_g levels as all d orbitals are not interacting to the same extent with the six point charges (O^{2-} ions) located on the $+x$, $-x$, $+y$, $-y$, $+z$ and $-z$ axes, respectively [15]. Hence, e_g orbitals ($x^2 - y^2$, z^2) lying along the axes get more destabilized than t_{2g} orbitals (xy , xz , yz) lying between the axes. Mn doping in the BFO lattice induce distortions in local Fe^{3+} crystal field, and c/a tetragonality ratio is increased. The arrangement of the ligands (O^{2-} ions) around the metal ion changes leading into further splitting of the t_{2g} states into doubly degenerate orbitals (xz , yz) and singly degenerate (xy) orbital while e_g orbitals split into lower energy orbital (z^2) and higher energy ($x^2 - y^2$) orbital which cumulatively broaden 3d states. In addition, O^{2-} 2p states move away from Fermi level as suggested by band structure calculation leading to larger forbidden gap due to the structure strain and symmetry lowering [5].

Fourier Transform Infrared (FTIR) Study

In addition to Raman spectroscopy and UV–visible transmission studies, Fourier transform infrared (FTIR) spectroscopy is also employed to reveal the details of molecular structure change in BFO thin film with Mn doping. Figure 4 exhibits the FTIR spectra of BFMO thin film with varying Mn concentrations from 0 to 20 % in the wavelength range $400\text{--}1000\text{ cm}^{-1}$. Clearly visible two strong and broad absorption bands in the region $420\text{--}470\text{ cm}^{-1}$ and $480\text{--}680\text{ cm}^{-1}$ in the FTIR spectra signify the

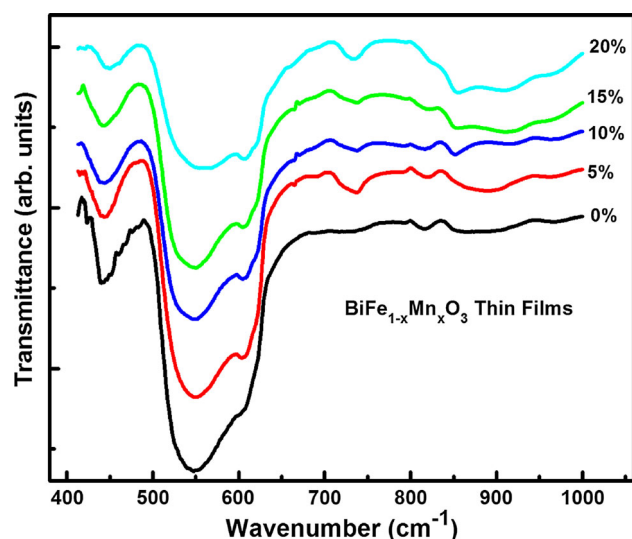


Fig. 4 FTIR spectra of BFMO thin film samples with varying concentrations of Mn dopant (0–20 mol %)

characteristic perovskite structure of all prepared samples. These bands are broad due to possible overlapping of nearly bismuth oxide and iron oxide absorption bands [19].

A small absorption band at 625 cm^{-1} corresponding to bending modes of the vibrations of bismuth oxide is clearly evident as a shoulder in Fig. 4 [19, 29], whereas weak absorption band around 740 cm^{-1} in the FTIR spectra of BFMO thin films is clearly seen in Fig. 4 which corresponds to anti-symmetric Mn–O–Mn stretching vibrations, indicating the Mn dopant incorporation into the host BFO lattice [30]. To extract more hindered information from these broad characteristic bands of the FTIR spectra, de-convolution in Gaussian components is employed using Peakfit-v4 software for all samples [19]. The de-convolution of the complex spectral region ($420\text{--}470\text{ cm}^{-1}$) and ($480\text{--}680\text{ cm}^{-1}$) into components bands is done using second-derivative analysis method which can highpoint the small differences in IR spectrum [31, 32]. De-convoluted spectra with their respective second-derivative plot are shown in Fig. 5a–e for $\text{BiFe}_{1-x}\text{Mn}_x\text{O}_3$ thin films with $x = 0, 0.05, 0.1, 0.15$ and 0.2 , respectively. The absorption band in $420\text{--}470\text{ cm}^{-1}$ region is resolved into two peaks. A strong mode at 443 cm^{-1} corresponding to O–Fe–O bending vibrations of the octahedral FeO_6 group in the perovskite structure [29, 33] and a weak band centred at 460 cm^{-1} due to the BiO_6 octahedral structure unit [34] in BFO thin film are observed (Fig. 5a).

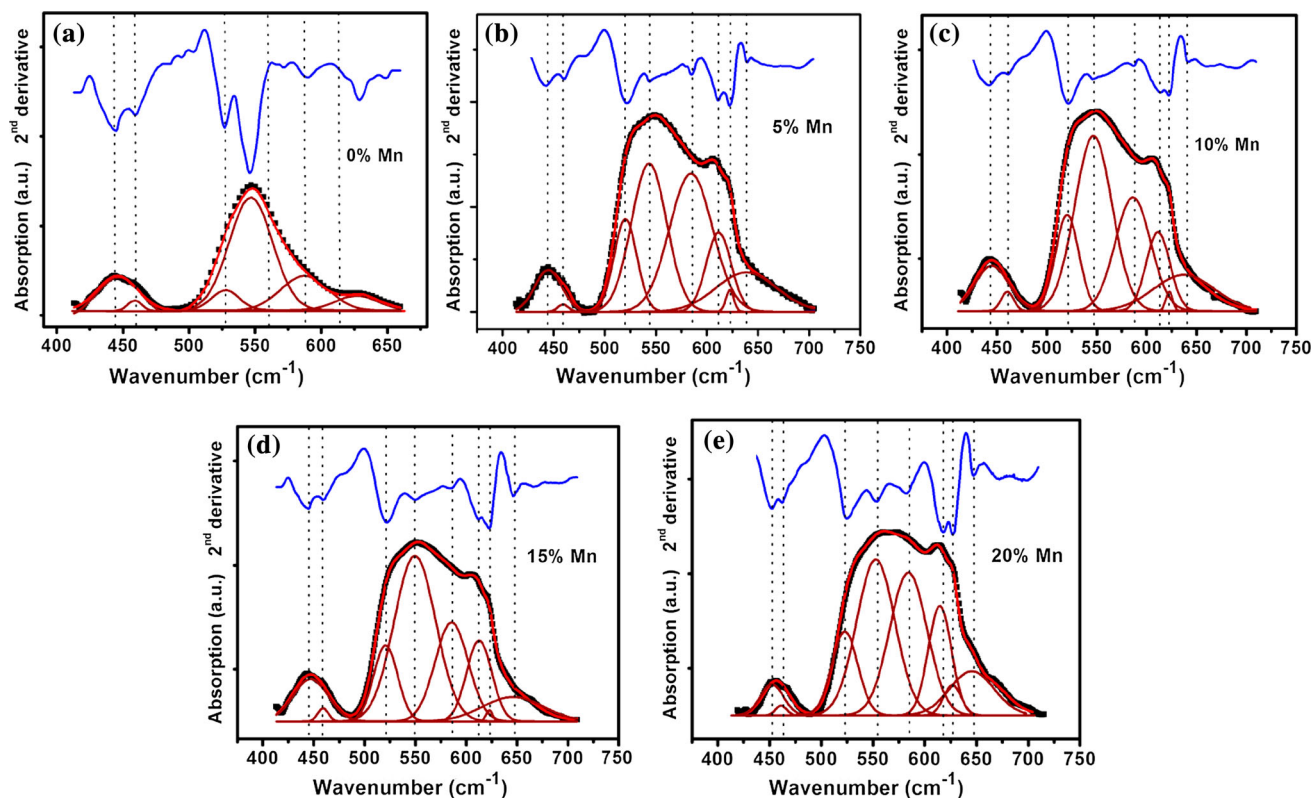


Fig. 5 De-convoluted FTIR spectra of **a** BiFeO_3 , **b** $\text{BiFe}_{0.95}\text{Mn}_{0.05}\text{O}_3$, **c** $\text{BiFe}_{0.90}\text{Mn}_{0.10}\text{O}_3$, **d** $\text{BiFe}_{0.85}\text{Mn}_{0.15}\text{O}_3$ and **e** $\text{BiFe}_{0.80}\text{Mn}_{0.20}\text{O}_3$ thin film in $420\text{--}700\text{ cm}^{-1}$ wavelength region. Black dots: raw FTIR data,

red line: theoretical fitting, wine line: de-convoluted peaks and blue line: second-derivative plot (Color figure online)

A small shift is observed in the IR active mode centred at 443 cm^{-1} towards higher wavenumber (up to 451 cm^{-1}) with increasing Mn doping concentration (up to 20 %) and is attributed to disorders in effective coordination number and the increase in bond length on Mn substitution at Fe sites in BFO lattice. A striking difference is observed in the de-convoluted FTIR spectra of BFO and BFMO thin films in spectral range $480\text{--}680\text{ cm}^{-1}$. This spectral region is resolved into four absorption bands for BFO film, whereas is de-convoluted into six bands for BFMO thin films. The four peaks—centred at 520 cm^{-1} corresponds to the Bi–O bond in the BiO_6 octahedral structure unit [34], 545 cm^{-1} related to the Fe–O stretching vibration present in the FeO_6 octahedral unit [34], 585 cm^{-1} assign to the out of phase vibrations of basis atoms of oxygen normal to the [111] plane of the rhombohedral BFO [15] and 625 cm^{-1} with weak intensity corresponds to bending modes of vibrations of bismuth oxides [35]—are obtained in the de-convoluted FTIR spectra of BFO thin film (Fig. 5a). A significant shift in the FTIR mode related to Fe–O stretching vibration from 545 cm^{-1} to 554 cm^{-1} is observed with increasing Mn doping concentration 0–20 % in BFO thin film (Fig. 5a–e) owing to substitution of Mn ions having relatively smaller ionic mass at the Fe sites in BFO lattice, as absorption wavenumber ($\bar{\nu}$) of stretching vibration depends on both the force constant between the two atoms (k) and relative masses of bonding atoms (m_1) and (m_2) and is given by the Hooke's law equation [36].

$$\bar{\nu} = \frac{1}{2\pi c} \left[k \left(\frac{m_1 + m_2}{m_1 m_2} \right) \right]^{1/2},$$

where c is the velocity of light. However, the formation of parasite phases including manganese oxides cannot be ruled out as the two additional modes at 610 and 640 cm^{-1} corresponding to Mn–O vibrations of bivalent manganese ions are also observed in the de-convoluted FTIR spectra of BFMO thin film in comparison to BFO thin film [37].

Conclusion

Single-phase BiFeO_3 and Mn-doped BiFeO_3 perovskite thin films were deposited on cost-effective corning glass and ITO-coated corning glass substrates by simple CSD technique with improved optical properties. Partial structural transformation of BFO thin films from rhombohedral to tetragonal symmetry with continuous increase in Mn doping concentration was confirmed by Le-Bail extraction fitting of XRD pattern and Gaussian Peak de-convolution of Raman spectra. Observed evolution in Raman phonon modes confirms the gradual occurrence of tetragonal phase with Mn doping and displays strong Jahn–Teller distortion.

Optical energy band gap is found to be blue shifted from 2.53 ± 0.01 to $2.87 \pm 0.01\text{ eV}$ with increasing Mn doping content in BFO thin film and is attributed to the local symmetry lowering and local induced strain in Fe^{3+} environment. De-convolution of FTIR absorption spectra in complex wavelength region ($420\text{--}470\text{ cm}^{-1}$) and ($480\text{--}680\text{ cm}^{-1}$) with second-derivative analysis for BFMO thin film samples further confirmed the lattice distortion owing to Mn substitution in BFO host lattice.

Acknowledgements Authors are thankful to the Department of Science & Technology (DST), Government of India for the financial support to carry out the work. One of the authors (SG) is thankful to the University of Delhi for the research fellowship (UTA).

References

1. Eerenstein W, Mathur ND, Scott JF (2006) Multiferroic and magnetoelectric materials. *Nature* 442:759–764
2. Ramesh R, Spaldin NA (2007) Multiferroics: progress and prospects in thin films. *Nat Mater* 6:21–29
3. Uniyal P, Yadav KL (2009) Observation of the room temperature magnetoelectric effect in Dy doped BiFeO_3 . *J Phys: Condens Matter* 21:012205(1)–012205(4)
4. Allibe J, Robin KB, Jacquet E, Infante IC, Fusil S, Carrétéro C, Reverchon JL, Marcilhac B, Creté D, Mage JC, Barthélémy A, Bibes M (2010) Optical properties of integrated multiferroic BiFeO_3 thin films for microwave applications. *Appl Phys Lett* 96:182902(1)–182902(3)
5. Chen P, Podraza NJ, Xu XS, Melville A, Vlahos E, Gopalan V, Ramesh R, Schlom DG, Musfeldt JL (2010) Optical properties of quasi-tetragonal thin films. *Appl Phys Lett* 96:131907(1)–131907(3)
6. Vengalis B, Devenson J, Oginskis AK, Lisauskas V, Anisimovas F, Butkute R, Dapkus L (2009) Optical and electrical properties of Nd-doped BiFeO_3 thin films and heterostructures. *Phys Status Solidi C* 6(12):2746–2749
7. Karimi S, Reaney IM, Han Y, Pokorny J, Sterianou I (2009) Crystal chemistry and domain structure of rare-earth doped BiFeO_3 ceramics. *J Mater Sci* 44:5102–5112
8. Kan D, Suchoski R, Fujino S, Takeuchi I (2009) Combinatorial investigation of structural and ferroelectric properties of A- and B-site co-doped BiFeO_3 thin films. *Integr Ferroelect* 111:116–124
9. Rabe KM (2005) Theoretical investigations of epitaxial strain effects in ferroelectric oxide thin films and superlattices. *Curr Opin Solid State Mater Sci* 9:122–127
10. Kharel P, Talebi S, Ramachandran B, Dixit A, Naik VM, Sahana MB, Sudakar C, Naik R, Rao MSR, Lawes G (2009) Structural, magnetic, and electrical studies on polycrystalline transition-metal-doped BiFeO_3 thin films. *J Phys: Condens Matter* 21:036001(1)–036001(6)
11. Chen P, Xu X, Koenigsmann C, Santulli AC, Wong SS, Musfeldt JL (2010) Size-dependent infrared phonon modes and ferroelectric phase transition in BiFeO_3 nanoparticles. *Nano Lett* 10:4526–4532
12. Jaiswal A, Das R, Maity T, Vivekanand K, Adyanthaya S, Poddar P (2010) Temperature-dependent Raman and dielectric spectroscopy of BiFeO_3 nanoparticles: signatures of spin-phonon and magnetoelectric coupling. *J Phys Chem C* 114:12432–12439
13. Kumar A, Scott JF, Katiyar RS (2011) Electric control of magnon frequencies and magnetic moment of bismuth ferrite thin films at room temperature. *Appl Phys Lett* 99:062504(1)–062504(3)

14. Hermet P, Goffinet M, Kreisel J, Ghosez P (2007) Raman and infrared spectra of multiferroic bismuth ferrite from first principles. *Phys Rev B* 75:220102(1)–220102(4)
15. Tütüncü HM, Srivastava GP (2008) Electronic structure and lattice dynamical properties of different tetragonal phases of BiFeO₃. *Phys Rev B* 78:235209(1)–235209(10)
16. Lahmar A, Habouti S, Dietze M, Solterbeck CH, Souni ME (2009) Effects of rare earth manganites on structural, ferroelectric, and magnetic properties of BiFeO₃ thin films. *Appl Phys Lett* 94:012903(1)–012903(3)
17. Reddy VR, Kothari D, Gupta A, Gupta SM (2009) Study of weak ferromagnetism in polycrystalline multiferroic Eu doped bismuth ferrite. *Appl Phys Lett* 94:082505(1)–082505(3)
18. Yuan GL, Or SW, Chan HL (2007) Structural transformation and ferroelectric–paraelectric phase transition in Bi_{1-x}LaxFeO₃ (x = 0–0.25) multiferroic ceramics. *J Phys D Appl Phys* 40:1196–1200
19. Bhushan B, Wang Z, Tol JV, Dalal NS, Basumallick A, Vasanthacharya NY, Kumar S, Das D (2012) Tailoring the magnetic and optical characteristics of nanocrystalline BiFeO₃ by Ce doping. *J Am Ceram Soc* 95:1985–1992
20. Mishra DK, Qi X (2010) Energy levels and photoluminescence properties of nickel-doped bismuth ferrite. *J Alloys Compd* 504:27–31
21. Gupta S, Sharma A, Tomar M, Gupta V, Pal M, Guo R, Bhalla A (2012) Piezoresponse force microscopy and vibrating sample magnetometer study of single phased Mn induced multiferroic BiFeO₃ thin film. *J Appl Phys* 111:064110(1)–064110(6)
22. Gupta S, Tomar M, James AR, Gupta V. Ce-doped bismuth ferrite thin films with improved electrical and functional properties. *J Mater Sci*. doi:10.1007/s10853-014-8243-y
23. Kothari D, Reddy VR, Sathe VG, Gupta A, Banerjee A, Awasthi AM (2008) Raman scattering study of polycrystalline magneto-electric BiFeO₃. *J Magn Magn Mater* 320:548–552
24. Singh MK, Ryu S, Jang HM (2005) Polarized Raman scattering of multiferroic BiFeO₃ thin films with pseudo-tetragonal symmetry. *Phys Rev B* 72:132101(1)–132101(4)
25. Szafraniak I, Polomska M, Hilczer B, Pielaszkowski A, Kepinski L (2007) Characterization of BiFeO₃ nanopowder obtained by mechanochemical synthesis. *J Eur Ceram Soc* 27:4399–4402
26. Yuan GL, Or SW, Chan HL (2007) Raman scattering spectra and ferroelectric properties of Bi_{1-x}NdxFeO₃ (x = 0 – 0.2) multiferroic ceramics. *J Appl Phys* 101:064101(1)–064101(5)
27. Carrón LM, Andrés AD, Lope MJM, Casais MT, Alonso JA (2002) Raman phonons as a probe of disorder, fluctuations, and local structure in doped and undoped orthorhombic and rhombohedral manganites. *Phys Rev B* 66:174303(1)–174303(8)
28. Kartopu G, Lahmar A, Habouti S (2008) Observation of structural transitions and Jahn–Teller distortion in LaMnO₃-doped BiFeO₃ thin films. *Appl Phys Lett* 92:151910(1)–151910(3)
29. Farhadi S, Zaidi M (2009) Bismuth ferrite (BiFeO₃) nanopowder prepared by sucrose-assisted combustion method: a novel and reusable heterogeneous catalyst for acetylation of amines, alcohols and phenols under solvent-free conditions. *J Mol Catal A* 299:18–25
30. Chertihin GV, Andrews L (1997) Reactions of laser-ablated manganese atoms with dioxygen. Infrared spectra of MnO, OMnO, Mn(O₂), (MnO)₂, and higher oxide complexes in solid argon. *J Phys Chem A* 101:8547–8553
31. Popescu MC, Filip D, Vasile C, Cruz C, Rueff JM, Marcos M, Serrano JL, Singurel G (2006) Characterization by fourier-transform infrared spectroscopy (FT-IR) and 2D IR correlation spectroscopy of PAMAM dendrimer. *J Phys Chem B* 110(29):14198–14211
32. Priyam A, Blumling DE, Knappenberger KL (2010) Synthesis, characterization, and self-organization of dendrimer-encapsulated HgTe quantum dots. *Langmuir* 26(13):10636–10644
33. Rao GVS, Rao CNR, Ferraro JR (1970) Infrared and electronic spectra of rare earth perovskites: ortho-chromites, -manganites and -ferrites. *Appl Spectrosc* 24:436–445
34. Som KK, Molla S, Bose K, Chaudhury BK (1992) Nonlinear physical properties of amorphous Bi₄Sr₃Ca₃Cu_yO_x semiconducting oxides with y between 0 and 5. *Phys Rev B* 45:1655–1659
35. Azama A, Jawad A, Ahmed AS, Chamanb M, Naqvi AH (2011) Structural, optical and transport properties of Al³⁺ doped BiFeO₃ nanopowder synthesized by solution combustion method. *J Alloys Compd* 509:2909–2913
36. Burke JT (1997) IR spectroscopy or Hooke’s law at the molecular level—a joint freshman physics-chemistry experience. *J Chem Edu* 74:1213
37. Buciuman F, Patcas F, Craciun R, Zahn DRT (1999) Vibrational spectroscopy of bulk and supported manganese oxides. *Phys Chem Chem Phys* 1:185–190